Stratigraphic influence on emplacement and 3-dimensional structure of a large mafic sill in sedimentary strata

Olivier Galland [1], Anna M. R. Sartell [2,3], Rafael Kenji Horota [3,4], Hans Jørgen Kjøll [1,5], Jonathan J. S. Runge [6], Ivar Midtkandal [5], Kim Senger [3]

[1] Njord Centre, Department of Geosciences, University of Oslo, Norway

[2] Department of Geosciences and Geography, University of Helsinki, PO Box 64, Gustaf Hällströmin katu 2, 00014 Helsinki, Finland

[3] Department of Arctic Geology, The University Centre in Svalbard, PO Box 156, 9171 Longyearbyen, Norway

[4] Department of Earth Science, University of Bergen, Allegaten 41, 5020, Bergen, Norway

[5] Tectonostratigraphic Research Group, Department of Geosciences, University of Oslo, Norway

[6] Mineral Resources Authority, Imaneq 4, 3900, Nuuk, Greenland

This paper has been peer reviewed and has been accepted for publication in Basin Research.

Abstract

Sills are fundamental elements of volcanic plumbing systems emplaced in sedimentary basins. Even though sills are commonly considered simple, planar concordant igneous sheets, they are actually complex 3-dimensional objects. Detailed knowledge of the 3D structure of sills and their host rocks is of primary relevance to better constraining the emplacement mechanisms and the impacts of sills on sedimentary basins. This study describes the results of 3-dimensional geological mapping of a large (~14×9 km), well-exposed Early Cretaceous dolerite sill in Central Spitsbergen, Svalbard, Arctic Norway, using a combination of digital outcrop modelling and field mapping. The sill was emplaced within Upper Palaeozoic sedimentary formations of Svalbard. It is made of distinct segments emplaced at different stratigraphic levels of the host rock stratigraphy. The mapping shows a clear stratigraphic control on the intrusion morphology. Sill segments emplaced at the boundary between two formations, which marks a strong lithological and rheological boundary, are straight and concordant. Conversely, segments emplaced within a more homogeneous formation exhibit more irregular, locally discordant shapes. The sill segments emplaced at distinct stratigraphic levels are connected by steeply dipping steps, which formed through dilatant shearing between the tips of the sill segments. The preferred NW-SE orientation of the steps and the thinning of the sill towards the SE suggests a propagation direction of the magma towards the SE. Our study shows how 3-dimensional knowledge of igneous intrusions is key for revealing their emplacement mechanisms.

1 Introduction

Sills are fundamental elements of volcanic plumbing systems emplaced in sedimentary basins (e.g., Planke et al., 2005; Magee et al., 2016; Polteau et al., 2016; Galland et al., 2018; Lombardo et al., 2024). Their potential effects on sedimentary basins and subsurface rocks are widely recognized on both local and regional scales (e.g., Einsele et al., 1980; Senger et al., 2017; Spacapan et al., 2018). Large sub-horizontal sill intrusions emplaced in organic-rich shale formations can trigger rapid maturation of organic matter (e.g., Aarnes et al., 2010; Iyer et al., 2017; Spacapan et al., 2018) and the generation of large volumes of methane and carbon dioxide (Svensen et al., 2004; Aarnes et al., 2010; Galerne and Hasenclever, 2019). The catastrophic release of these gases into the atmosphere has triggered extreme climate change and mass extinctions (Courtillot and Renne, 2003; Svensen et al., 2004; Svensen et al., 2009). Conversely, sills can also act as fractured reservoirs for water or hydrocarbons (Chevallier et al., 2001; Chevallier et al., 2004; Spacapan et al., 2020a; Spacapan et al., 2020b; Rabbel et al., 2021) or as reservoir seals (de Miranda et al., 2018). Additionally, groundwater exploration and CO_2 sequestration is affected by the presence of sills in sedimentary basins because of the fracturing within the sills or in their host rock (Chevallier et al., 2001; Senger et al., 2013; Senger et al., 2017).

By definition, sills are concordant, straight igneous sheets, following strata of the host rock. However, in reality, sills are made of concordant segments with locally discordant parts, so that sills are complex 3-dimensional (3D) objects (e.g., Planke et al., 2005; Galland et al., 2018; Galland et al., 2019; Magee et al., 2019). The general concordant nature of sills leads to a general consensus that their emplacement is controlled to a large extent by the layering of the host rocks (Kavanagh et al., 2006; Thomson and Schofield, 2008; Galland et al., 2018). At large scale, 3D seismic data and field geological observations on seismic-scale outcrops show that sills may consist of concordant sill segments, emplaced at different stratigraphic levels,

connected by steps or broken bridges, the orientation of which may indicate the propagation direction of the intrusion (Figure 1) (e.g., Thomson and Hutton, 2004; Hansen and Cartwright, 2006; Thomson, 2007; Hutton, 2009; Schofield et al., 2012; Magee et al., 2016; Schmiedel et al., 2017; Galland et al., 2019; Magee et al., 2019). Field observations of Rabbel et al. (2021) and Kjenes et al. (2022) also demonstrated that subtle morphological variations in sill geometry can significantly modify the fracture distribution both within and outside the intrusion. Thus, detailed knowledge of the 3D structure of sills and their host rocks is of primary relevance to better constraining the emplacement mechanisms and properties of sills and their surrounding strata.

During the last two decades, the main tool for studying the 3D architecture of igneous sills has been 3D seismic interpretation (e.g., Thomson and Hutton, 2004; Hansen and Cartwright, 2006; Thomson, 2007; Schofield et al., 2012; Magee et al., 2016; Schmiedel et al., 2017; Lombardo et al., 2024). Most of these studies provide additional evidence that sills in 3D may consist of lobes or segments (Figure 1B), sometimes connected by steps or broken bridges, the orientation of which may indicate the propagation direction of the intrusion (e.g., Thomson and Hutton, 2004; Hutton, 2009; Magee et al., 2019). Nevertheless, even though 3D seismic images of sills are spectacular, the scales of sill-related structures are commonly below seismic resolution (Mark et al., 2018; Rabbel et al., 2018), such that key elements might be invisible in the seismic data. Conversely, field geological mapping appears limited to reconstruct the 3D structure of large igneous sills. Most exceptional exposures of sills are displayed along 2-dimensional (2D) sections (Figure 1A) (Hutton, 2009; Eide et al., 2016; Rabbel et al., 2018; Galland et al., 2019), so that the third dimension is challenging to infer. In the Karoo Basin, South Africa, the top surfaces of some sills are exposed in 3D (Polteau et al., 2008; Galerne et al., 2011), but the overburden is eroded and the host rock below the sills are scree-covered.

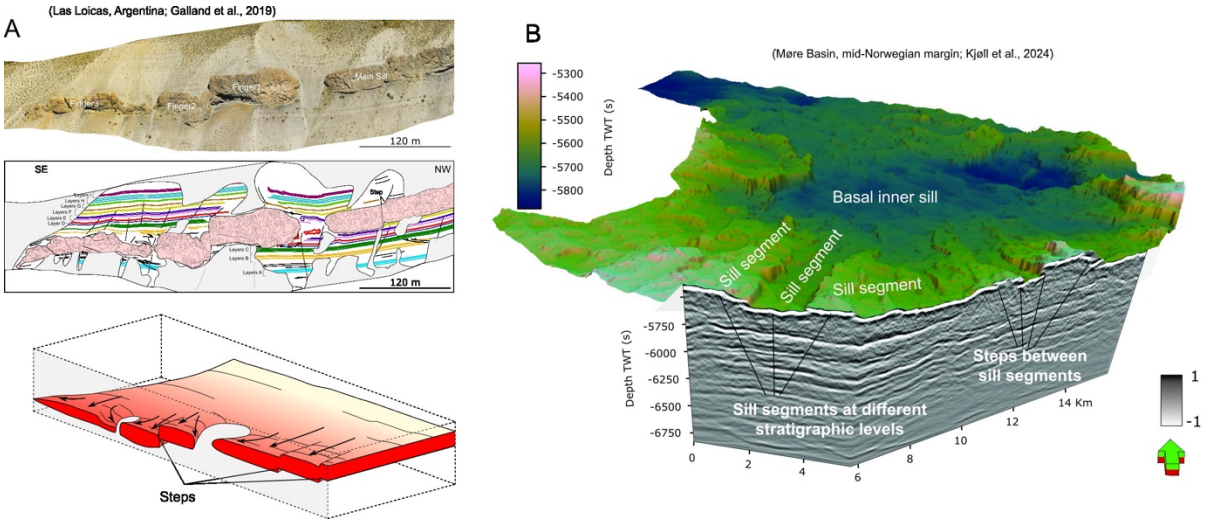

Figure 1. A. Orthorectified image (top) and structural interpretation (middle) of outcropping igneous fingers emplaced in organic-rich shale, Las Loicas, Neuquén Basin, Argentina (Galland et al., 2019). Bottom: schematic 3D block diagram of the structure and emplacement of the sill and fingers. B. 3D depth map of a sill that show fingers emplaced at different stratigraphic levels, providing a stepped expression in the seismic cross-section and on the corresponding mapped surface. Individual fingers are ca 2 km wide and ca 5-10 km long. Sill is located in Møre Basin on mid-Norwegian margin and emplaced into Cretaceous aged strata dominated by bathyal mudstones. Details of the seismic survey are described by Kjøll et al. (2024). The color bar for the seismic profile is displayed such that black denotes an increase in acoustic impedance. Scientific color bar for the 3D surface of the sill is "Batlow" from (Crameri et al., 2020)

This study describes the results of a mapping campaign of the peninsula separating Ekmanfjorden from Dicksonfjorden in central Spitsbergen, Svalbard, Arctic Norway (Figure 2). Here a large Early Cretaceous dolerite sill is exposed in steep, near-vertical cliffs (see section 4) that we mapped using a combination of digital outcrop modelling and field mapping. The mountain massif is deeply eroded by glaciers creating valleys, which in turn allow 3D-reconstruction of the sill and its relationship with the host rock strata.

2 Geological setting

The study area is a mountainous peninsula outcropping in the northern part of Isfjorden separating Ekmanfjorden and Dicksonfjorden (Figure 2). The studied sill is a dolerite intrusion that belongs to the Diabasodden Suite (Dallmann, 1999; Maher, 2001; Senger et al., 2014a; Senger and Galland, 2022; Sartell et al., in press). The studied sill is exposed as discontinuous, small outcrops. However the mapping work presented in this paper and the similar geochemical compositions and U-Pb ages of the studied sill outcrops (Sartell, 2021; Sartell et al., in press) suggest that these represent discontinuous remnants of a large, continuous intrusion. The Diabasodden Suite is exposed throughout Svalbard (Figure 2) and comprises Early Cretaceous dolerite sills and dykes emplaced predominantly in heterogeneous host rocks including metamorphic basement, Paleozoic carbonates and Mesozoic shales (Senger et al., 2014b; Senger and Galland, 2022). Regionally, the Diabasodden Suite represents the Svalbard portion of the circum-Arctic High Arctic Large Igneous Province (HALIP; e.g., Maher, 2001; Senger and Galland, 2022; Sartell et al., in press).

The geological evolution of Svalbard is well covered in the literature (e.g., Steel and Worsley, 1984; Worsley, 2008; Dallmann, 2015; Olaussen et al., 2025), and includes several tectono-magmatic events affecting the host rocks. In this section we will focus on the rock formations outcropping in the study area (Figure 2), and the broader tectono-magmatic evolution of the area.

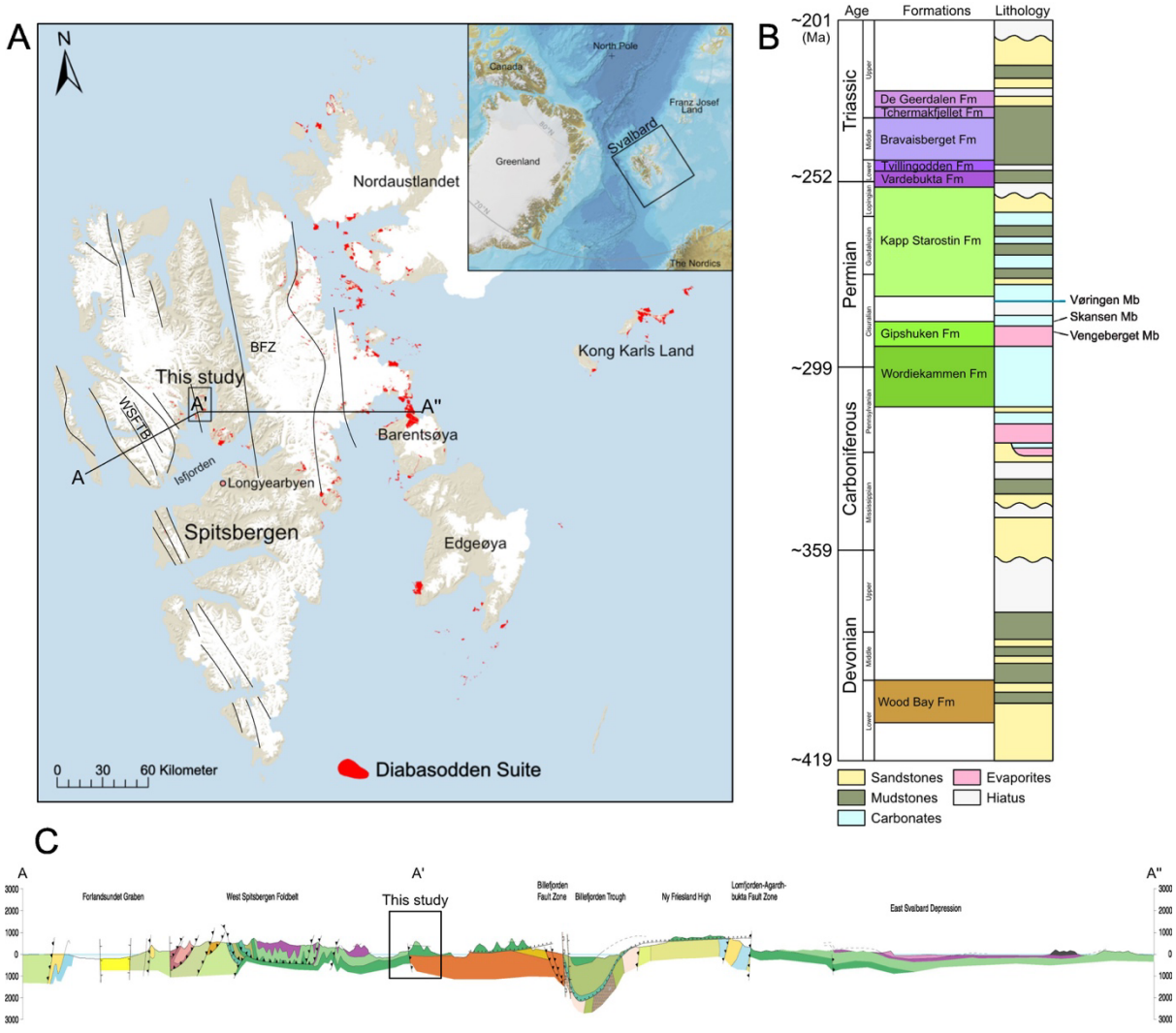

Figure 2. A. Map of Svalbard Archipelago, locating the study area (rectangle). White domains are glaciers. Red indicates distribution of dolerites of the Diabasodden Suite. The topographical map is based on the digital elevation model, glacier extent and land area from the Norwegian Polar Institute (2014b, a), and the extend of the Diabasodden Suite is modified from the Geological map of Svalbard (Norwegian Polar Institute, 2016). Inset: map of the Arctic locating Svalbard. The Arctic map is modified from the International Bathymetric Chart of the Arctic Ocean (IBCAO v 3.0) (Jakobsson et al., 2012). Black line locates cross section of C. BFZ: Billefjorden Fault Zone; WSFTB: Western Svalbard Fold and Thrust Belt. B. Stratigraphic column of study area, modified from Sorento et al. (2020) and Olaussen et al. (2025). C. Geological cross section located in A (Dallmann, 2014).

Following the Caledonian orogeny, the Devonian Old Red Sandstone succession, which includes the Wood Bay Formation (Figure 2B), was deposited in major fault-bounded basins exposed in northern Svalbard (Braathen et al., 2018). The Ellesmerian (locally called Svalbardian) compressional event affected Svalbard during the Late Devonian (Piepjohn, 2000). A tectonically stable platform was established from Late Carboniferous-Early Permian and lasted until the Late Jurassic. The transition from warm-water carbonates and evaporites of the Wordiekammen and Gipshuken formations, respectively (Blomeier et al., 2009; Ahlborn and Stemmerik, 2015) to cold-water carbonates of the Kapp Starostin Formation during the Permian was facilitated by Svalbard's rapid northward drift (Blomeier et al., 2013). The Gipshuken Formation exhibits two members that are prominent in the field: the lower Vengeberget Member dominated by evaporites, and the upper Skansen Member, dominated by carbonates (Sorento et al., 2020). Sub-aerial exposure and erosion, followed by an abrupt shift in facies towards brachiopod-dominated cool-water carbonates marks the lower boundary to the overlying Vøringen Member and spiculitic chert of the upper Artinskian – upper Permian Kapp Starostin Formation (Bond et al., 2018; Sorento et al., 2020).

Large intrusions of the Diabasodden Suite were emplaced in Triassic strata in the vicinity of the study area (Senger and Galland, 2022). The Triassic was dominated by siliciclastic deposition, beginning with Early Triassic deltaic to offshore Vikinghøgda/Tvillingodden formations sourced largely from west (i.e. Greenland) (Dallmann, 2015). The Middle Triassic organic-rich mudstones of the Botneheia Formation form a major host rock for the igneous intrusions of the Diabasodden Suite (Krajewski, 2013; Wesenlund et al., 2021; Senger and Galland, 2022). Subsequently, Late Triassic-Early Cretaceous sedimentation continued while Svalbard was moving northward.

168 The Early Cretaceous was marked by a shift in sedimentary patterns, associated with a
169 regional southward tilting of Svalbard. This was caused by major uplift to the north during the
170 Early Cretaceous, related to regional-scale thermal doming associated with HALIP magmatism
171 (Ineson et al., 2021).

172 A major regional erosion event removed most of the Upper Cretaceous strata (Maher,
173 2001). Reworked pollen of Middle to Late Cretaceous age indicate that Upper Cretaceous strata
174 were present in Svalbard in the past (Smelror and Larssen, 2016). Paleogene strata were
175 deposited in the Central Spitsbergen Basin, a sedimentary basin formed in the foreland of the
176 Paleogene West Spitsbergen transpressive fold-and-thrust belt located in the west (Bergh et al.,
177 1997). The entire igneous complex of the Diabasodden Suite was affected by this major
178 tectonic event, as evidenced by faulted and folded igneous intrusions at, for instance,
179 Festningen and Mediumfjellet. Neogene glaciations coupled with tectonic and glacio-isostatic
180 uplift developed hiatuses and deeply serrated topography which exposes the studied outcrops
181 (Lasabuda et al., 2021). Constraining the emplacement depth of the sills is complicated by
182 these factors.

183 Despite a long-lasting tectonic evolution in Svalbard, the study area is very little
184 affected by tectonic deformation, whereas it extends between two major structures (Figure 2C).
185 To the east, the Billefjorden Fault Zone (BFZ) is one of the best studied examples of long-lived
186 N-S trending structural lineaments affecting Svalbard (Bælum and Braathen, 2012). The BFZ
187 records strike-slip movement during the Caledonian orogeny, reverse movement during the
188 Late Devonian, normal movement during the Middle Carboniferous, and reverse re-activation
189 during the Paleogene. The Blomesletta Fault zone is a similar N-S striking fault zone that
190 crosses the study area (Figure 3). To the west, the study area is bounded by the West
191 Spitsbergen Fold and Thrust Belt (Figure 2). Dips in the study area are gently towards the
192 south, following regional uplift in the north during the Cretaceous.

3 Methods and data

Fieldwork involved mapping dolerite sill outcrops across the entire study area bounded by Ekmanfjorden, Dicksonfjorden and Syningsdalen (Figure 3) during three summer field expeditions (2019, 2020 and 2021). Place names are given where peaks are named, while unnamed peaks are referred to by their elevation in metres. Particular focus was on documenting contacts of the intrusion and identifying the stratigraphic level into which the dolerite body was emplaced. The mapping work integrated remote observations via drone surveys with field observations to complement, calibrate and ground-truth the drone data.

The drone surveys were designed and executed in order to generate digital outcrop models (DOM) of the study area using structure from motion and multiview stereopsis (SfM-MVS) photogrammetric processing (Westoby et al., 2012; Betlem et al., 2023). The drone used was a DJI Mavic 2 Pro quadcopter, with a standard 20 MegaPixel (MP) RGB camera with 1" CMOS (complementary metal oxide semiconductor) sensor. Photogrammetric processing of the drone images was performed using Agisoft Metashape following the workflow outlined by Betlem et al. (2023) (see also Bonali et al., 2020; Buckley et al., 2022), and the DOM is openly available (model Svalbox-DOM_2021-0058; Horota and Svalbox Team, 2024) through the Svalbox database (Senger et al., 2020; Betlem et al., 2023). The DOM was processed from 1886 photographs and covers an area of 56.2 km^2 with a pixel resolution of 11.4 cm/pix. Georeferencing of the DOM was done using the GPS positions of the drone recorded in the exif data of the photographs.

Using the combined DOM of the peninsula and observations from the field, the main contacts between the sedimentary formations (Wordiekammen, Gipshuken, and Kapp Starostin Formations, and the Vengeberget and Skansen Members of the Gipshuken Formation) and the intrusive body were mapped. Only areas where the contacts and boundaries were well-defined

and visible were marked, and scree-covered slopes were avoided. The detailed geological map was drawn using ArcGiS Pro (Figure 3). Additionally, the dolerite body thickness was measured on the DOMs in Agisoft Metashape, where both the lower and upper contacts of the sill were exposed. Spatial information from each image is included in the DOM, which allows the elevation between top and bottom sill contacts to be compared. At each location, several thickness measurements were made and averaged. In addition, we used LIME (version 3.0.1) to perform measurements of structural planes on the DOMs (Buckley et al., 2019), such as steps between sill segments (see section 4.2). A measurement with LIME consists of clicking three points on the plane, and LIME returns all the plane information such as dip and dip direction. To ensure precise measurements, we performed 10 measurements of each structure, and calculated the average plane.

4 Sill distribution and characteristics

This detailed mapping allowed us to constrain the shape of the studied sill and the stratigraphic levels at which it was emplaced at high resolution. We primarily recognized (1) concordant sill segments and (2) discordant steps and irregular segments.

4.1 Dominantly concordant sill segments

The largest dolerite outcrops correspond to large concordant sill segments. These segments occur as thick sheets that are laterally continuous up to 3 kilometres. We recognised several concordant sill segments emplaced at different stratigraphic levels.

The concordant sill segment emplaced in the deepest stratigraphic level is the intrusion that crops out west of Garborgnuten at peak 729 (Figure 4). The bottom intrusive contact was emplaced near the contact between the lower (Vengeberget) and upper (Skansen) members of

242 the Gipshuken Formation (Figure 4). The roof of this sill segment is unreachable, and we infer
243 from drone images that the overburden rocks of the sill are metamorphosed carbonates of the
244 upper (Skansen) member of the Gipshuken Formation.

245 We mapped several concordant segments emplaced along the stratigraphic contact
246 between the Gipshuken and Kapp Starostin formations. The largest segment makes the dolerite
247 plateau of Stjerthøgda that also extends to the south to Vengeberget (Figure 5). In the upper
248 parts of Stjerthøgda, we observed that the concordant sill segment was emplaced a few meters
249 below the boundary between the Gipshuken and Kapp Starostin formations. The sill exposed
250 at Blomesletta also appeared to be emplaced at a similar stratigraphic level (Figure 6). The sill
251 contact exposed at the northern end of Blomesletta is concordant with the stratigraphic contact
252 between the Gipshuken and Kapp Starostin formations (Figure 6A), whereas the sill contact
253 exposed at the southern end is discordant and cross cuts the chert deposits of the Kapp Starostin
254 Formation (Figure 6B). Note that the concordant dolerite segment at Blomesletta is located a
255 few meters above the boundary between the Gipshuken and Kapp Starostin formations (Figure
256 6A). The third sill segment emplaced at the stratigraphic contact between the Gipshuken and
257 Kapp Starostin Formations is well exposed at the summit of Peak 730 east of Meyerfjellet
258 (Figure 6C). South of Garborgnuten, on the other edge of the Kapitolbreen glacier, another
259 segment was emplaced at the same stratigraphic level (Figure 4). Finally, the segments at the
260 northwestern part of Rasmusdalen were also emplaced along the stratigraphic contact between
261 the Gipshuken and Kapp Starostin formations (Figure 3).
262

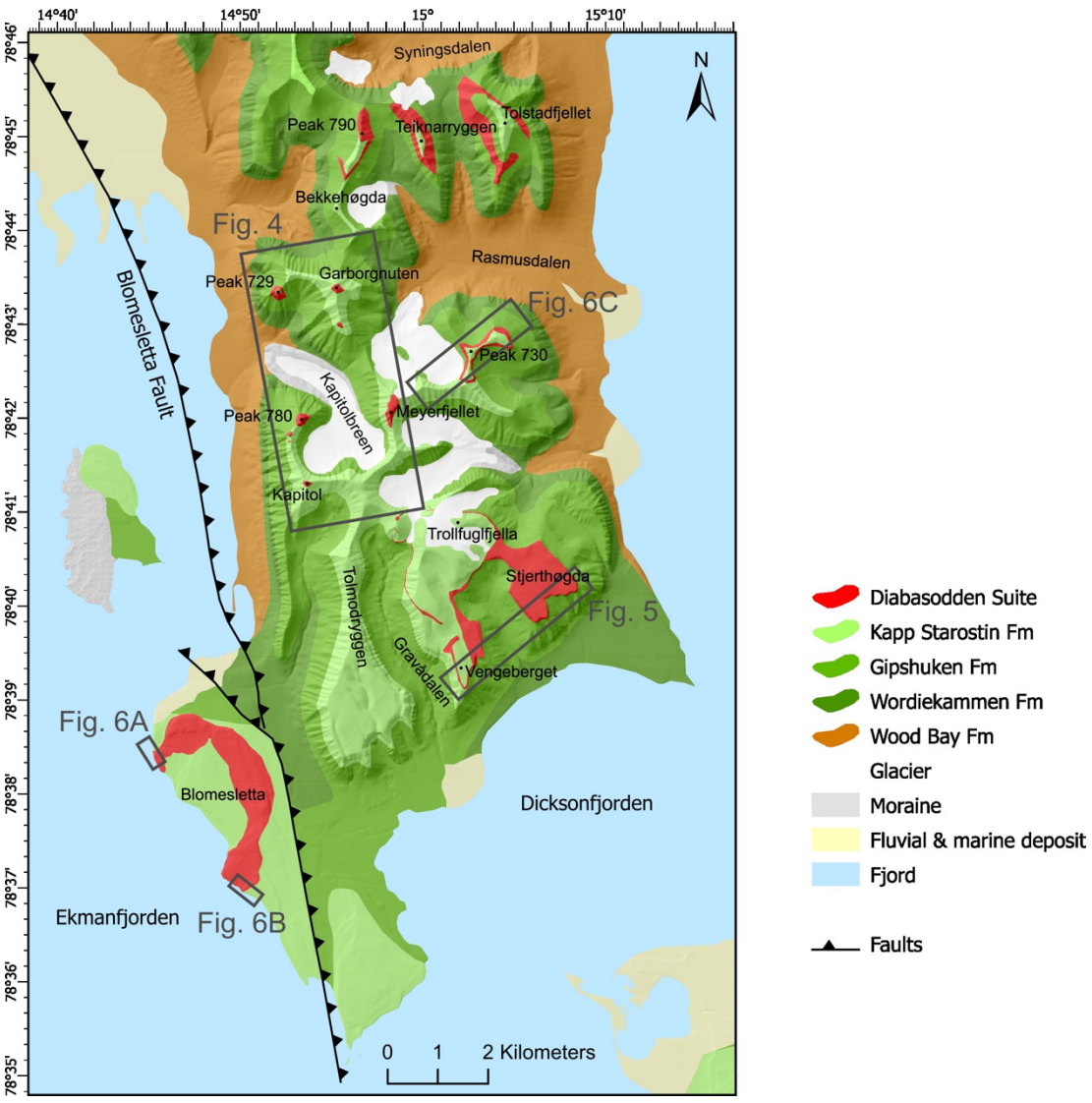

263

264 Figure 3. Detailed geological map of study area compiled from our field observations. The
265 topographical map is based on the digital elevation model, glacier extents and land area from
266 the Norwegian Polar Institute (2014b, a), and the extent of the Diabasodden Suite (red) is
267 modified from the Geological map of Svalbard (Norwegian Polar Institute, 2016), based on our
268 field observations. Grey boxes locate landscapes illustrated by Figures 4-6.

269

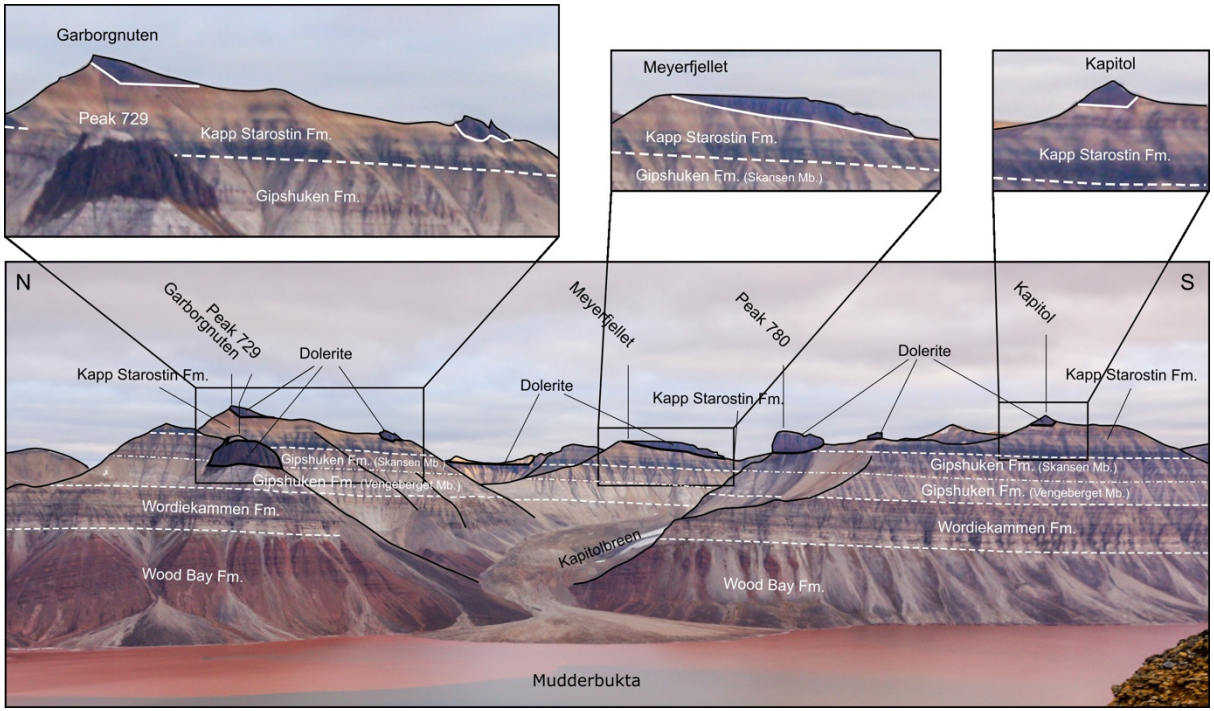

Figure 4. Bottom: Field photograph of western side of Garborgnuten, Peak 729, Meyerfjellet, Peak 780 and Kapitol mountains (location in Figure 3), seen from Kolosseum. White dashed lines locate stratigraphic contacts between the main lithostratigraphic units. Bold solid black lines indicate intrusive contacts of dolerite units. Top: zoomed in views of Garborgnuten, Meyerfjellet and Kapitol.

4.2 Discordant steps and irregular segments

In addition to the large concordant sill segments described above, our mapping highlighted discordant structures.

The bottom contacts of the sill segments emplaced within the Kapp Starostin Formation are irregular and only partly concordant. At the top of Garborgnuten, the bottom contact is concordant in its southern part and climbs obliquely in its northern part (upper left of Figure 4). This small segment may be connected to the dolerite outcropping to the south along the same ridge (Figure 4). At Meyerfjellet, the exposed bottom contact is straight but discordant with the host rock strata, gently dipping toward the south (Figure 4). Finally, at the top of Kapitol, the bottom contact is concordant in its northern part and climbs obliquely southward (Figure 4). Despite the limited extent of these outcrops, these observations suggest that the sill segments emplaced within the Kapp Starostin Formation are more irregular than the straight concordant segments emplaced at the stratigraphic contact between the Gipshuken and the Kapp Starostin formations.

Steeply-dipping to vertical sheets emerge from one edge of concordant sill segments (Figure 7). For example, the discordant step structure at the intrusion west of Garborgnuten (Peak 729; Figure 7C) accommodates a sharp transition from a thick concordant sill to a thin steeply dipping segment. On the eastern flank of Gravådalen, the concordant sill segment emplaced between the Gipshuken and the Kapp Starostin formations climbs as a step toward Vengeberget (Figure 7E). On both sides of the step, the units of the Kapp Starostin Formation can be recognised, however they are offset vertically: the layers of the Kapp Starostin Formation are higher above the concordant sill segment (left in Figure 7E) than in the section without the sill (right in Figure 7E). We infer that the step structure accommodates both upward propagation of the magma and the thickening of the concordant sill segments.

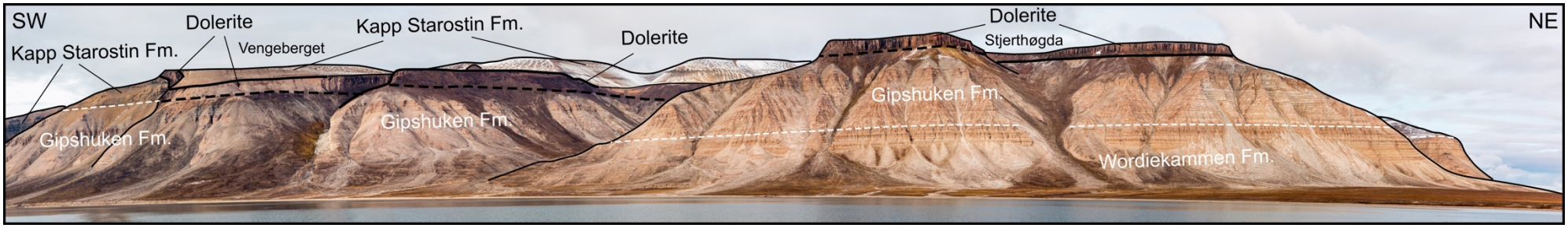

Figure 5. Field photograph of south-eastern side of the study area between Vengeberget and Stjerthøgda mountains. White dashed lines locate stratigraphic contacts between lithostratigraphic units. Thin solid black lines indicate observed intrusive contacts of the dolerite. Bold dashed black lines indicate inferred intrusive contacts of the dolerite. See location in Figure 3.

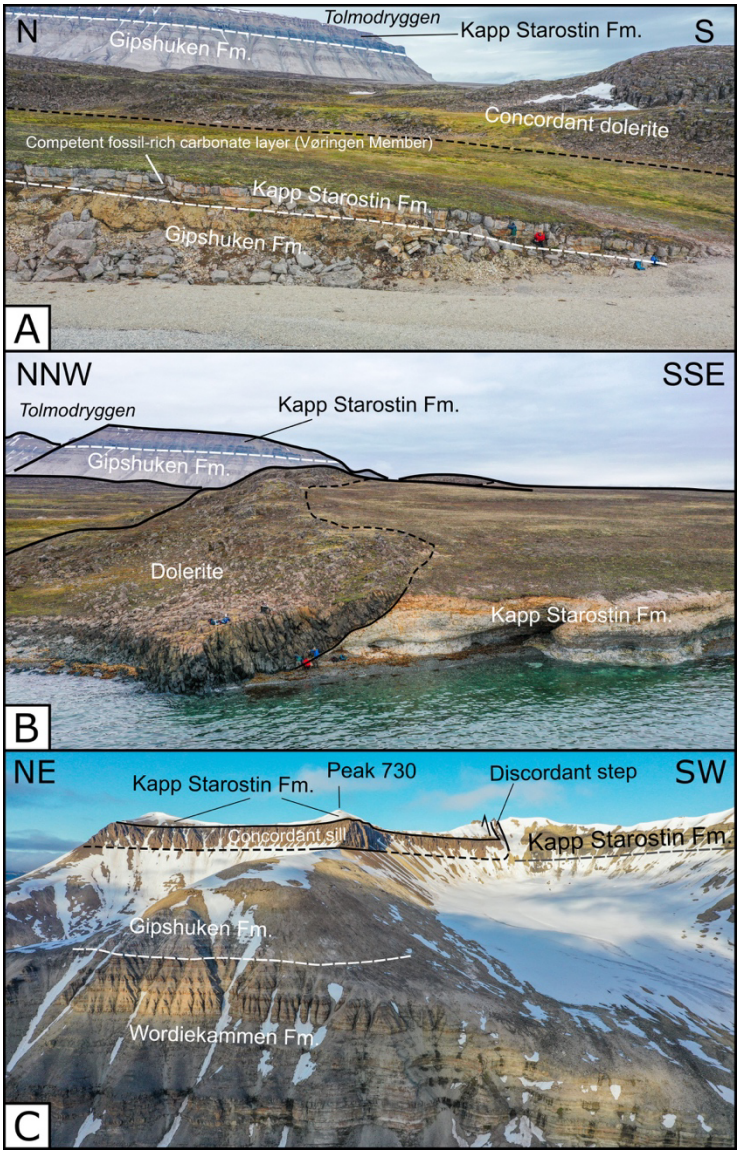

307

308 Figure 6. Field drone photographs of studied sill. A. Northern concordant contact along the
309 shore of Blomesletta. B. Southern discordant contact along the shore of Blomesletta. C. Drone
310 photograph of summit east of Meyerfjellet displaying an exposed concordant sill segment and
311 discordant step. Dashed white (and dark grey) lines locate stratigraphic contacts. Solid and
312 dashed black line locate established and inferred, respectively, intrusive contacts. See locations
313 in Figure 3.

314

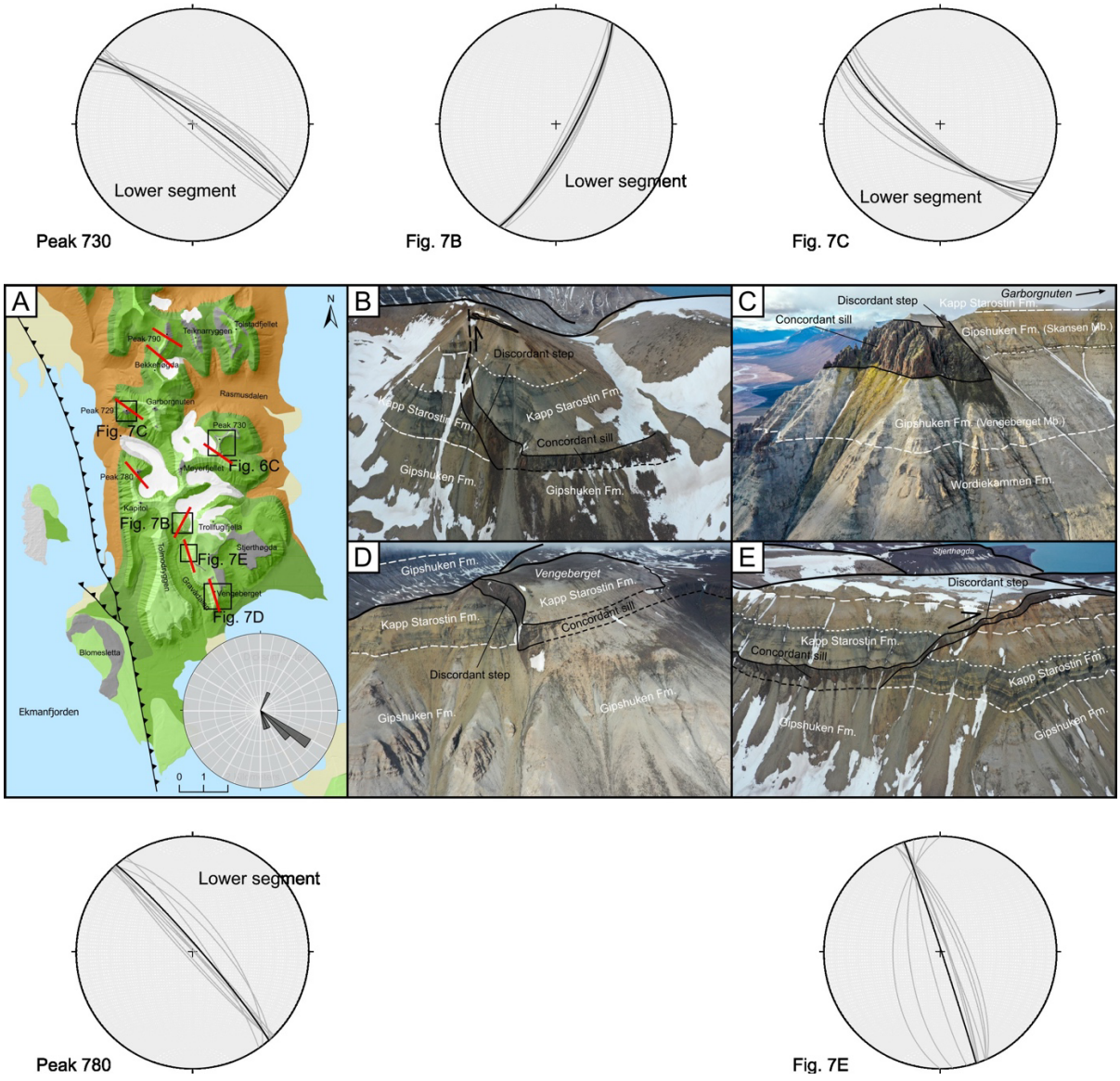

Figure 7. A. Simplified geological map of study area (same as Figure 3) locating field photographs of this figure and of Figure 6C. Red lines indicate location and orientation of intrusive steps. B. Drone photograph of exposed concordant sill segment and discordant step to the east of Trollfuglfjella. C. Drone photograph of well exposed concordant sill segment and discordant step to the west of Garbognuten mountain. D. Drone photograph of concordant sill segment and discordant step at Vengeberget. E. Drone photograph of concordant sill segment and discordant step northwest of Vengeberget. Text indicating igneous segments is in black font, text indicating host rock formation is in white font. **Stereograms**: display structural

measurements of the steps on DOM using LIME (see section 3). Grey lines correspond to plane measurements, black lines correspond to calculated average plane.

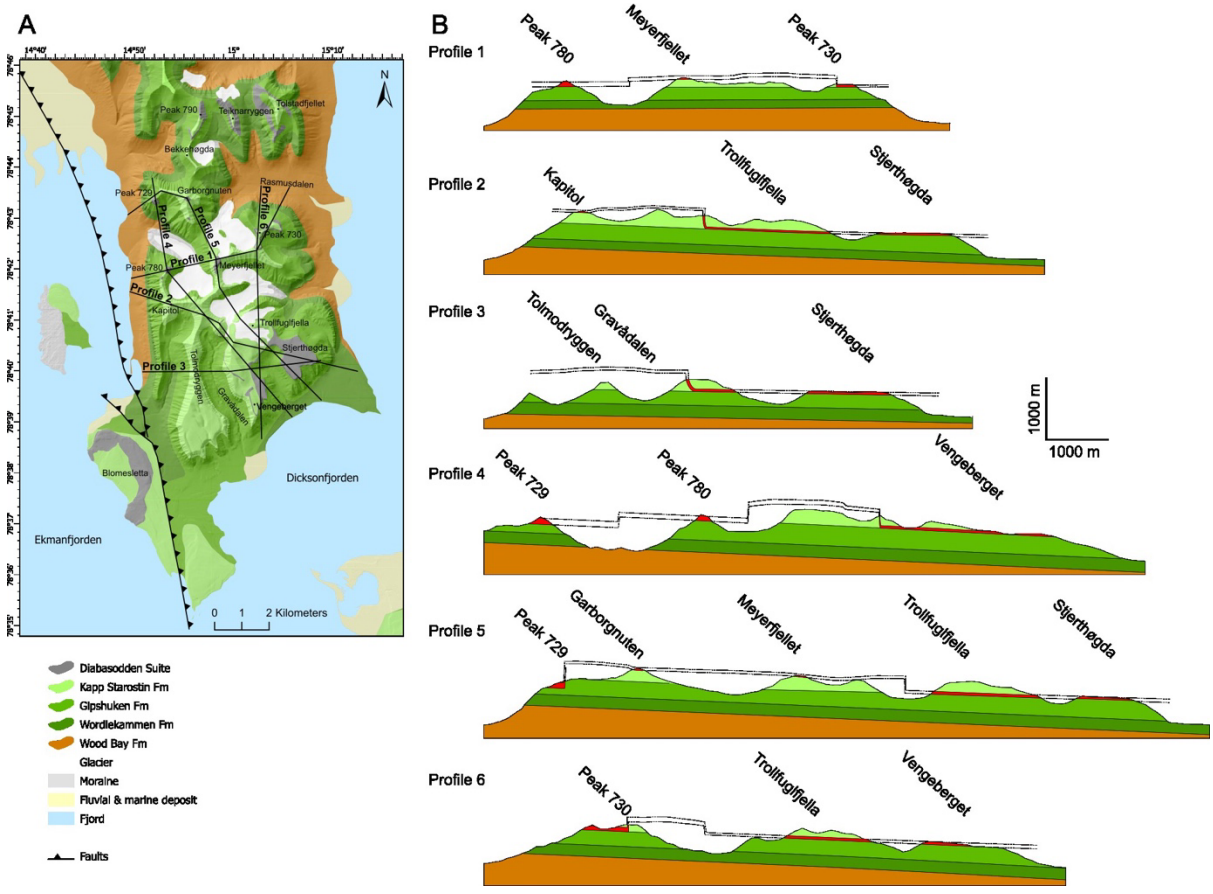

Figure 8. A. Geological map of the study area (same as Figure 3) locating geological cross sections of B. B. Geological cross sections constructed from the DOMs and geological field observations.

Structural measurements of the steps using LIME show that all measured steps are steeply dipping, or even vertical (step in Figure 7E). Note that the measured steps systematically dip towards the lower sill segment, i.e. the sill segment that feeds the step from below. The step at Vengeberget (Figure 7D) looks different than the others, with an apparent subvertical segment connected to the concordant segment emplaced at the stratigraphic contact between the Gipshuken and the Kapp Starostin formations. Further up, the step seems to bend

laterally, such that it exhibits a shallow dip. However, we could not do structural measurements of this step with LIME, because its 3-dimensional exposure is insufficient.

Mapped steps exhibit a predominant NW-SE orientation (Figure 7A).

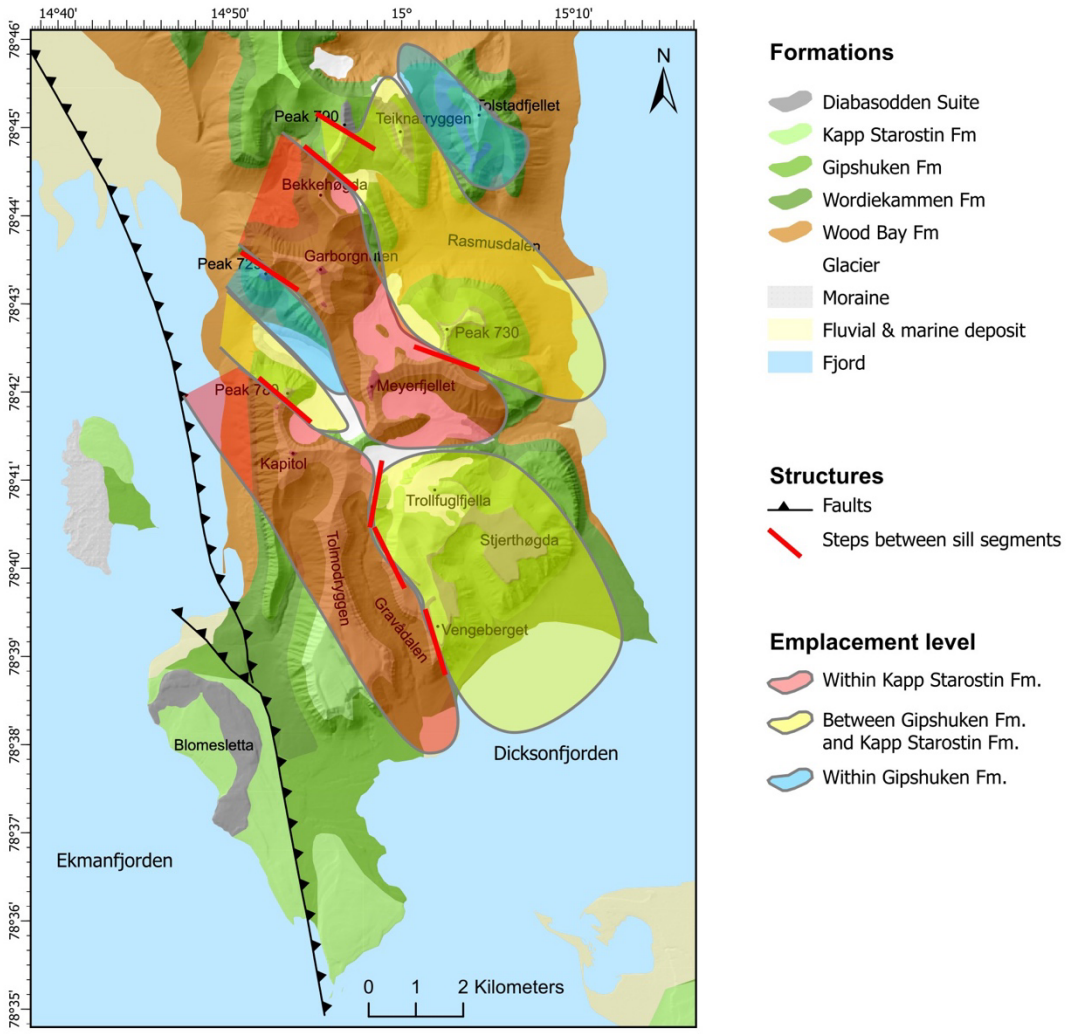

Figure 9. Geological map of study area (same as Figure 3) highlighting the interpolated sill segments with colours reflecting their stratigraphic level of emplacement to highlight the elongated lobe morphology of the segments.

4.3 Intrusion thickness

At Peak 729 (Figure 7C), Peak 780 and Peak 730 (Figure 6C), both the bottom and top contacts of the concordant sheets are well exposed. From NW to SE, the intrusion thickness at Peak 729 is 105 m, at Peak 790 the thickness is 96 m, and at Peak 730 the thickness is 70 m.

At Stjerthøgda, the bottom contact of the sill is well exposed locally, but the top contact is not preserved. Nevertheless, the Stjerthøgda plateau is flat and parallel to the exposed bottom contact. We assume that if significant erosion of the upper part of the sill took place, the Stjerthøgda plateau would not be so flat, but instead dissected by valleys. We consequently infer that the top of the Stjerthøgda plateau is a good proxy for the top contact of the sill exposed there, though it is a slight underestimate. The sill is 45 m thick along its southwestern edge and 36 m along its easternmost edge.

Along the eastern flank of Gravådalen, the top contact of the concordant sill is well exposed, but the bottom contact is covered (Figure 7B and E). Nevertheless, where the intrusion climbs to an inclined sheet, the overlying Kapp Starostin Formation is offset vertically (Figure 7B and E). We interpret that the offset is a good proxy for the thickness of the underlying concordant sheet (see interpretation section 5.3), and measure it to 42 m.

Finally, at the northern end of Gravådalen, the concordant sill segment emplaced between the Gipshuken Formation and the Kapp Starostin Formation exhibits a step, across which the Kapp Starostin Formation is vertically offset. Similarly to the estimate described above, the vertical offset of 42 m is assumed to be a good proxy of the thickness of the concordant sill segment. Note that due to local tilting related to the step formation, the offset estimate is likely less precise.

These measurements highlight a systematic thinning of the sill segments from the northwest to the southeast.

5 Interpretation and discussion

5.1 Continuity and structure of the sill

The studied sill crops out discontinuously near the top of several mountains, so that the continuity displayed in the geological cross sections of Figure 8 is an interpretation. Nevertheless, several elements support this interpretation: the mapped sill segments were emplaced at similar stratigraphic levels, the mapped steps provide a structural explanation of how sill segments emplaced at distinct stratigraphic levels may be connected (Figure 7), and the geochemical compositions and U-Pb ages of the studied sill segments are very similar (Sartell, 2021; Sartell et al., in press).

Note that the sill segment at Blomesletta was emplaced at the stratigraphic boundary between the Gipshuken and the Kapp Starostin formations (Figure 3, Figure 6), i.e. the same stratigraphic level as those of several segments of the mapped sill. Even though the sill at Blomesletta crops out at much lower elevations than the segments mapped high in the mountains, it is likely that the sill exposed at Blomesletta is part of the studied sill, but in an offset position due to the Blomesletta thrust fault (Blinova et al., 2013) in between the main peninsula and Blomesletta (Figure 3).

The distribution of the sill segments, their stratigraphic levels of emplacement, and the steps connecting them allows for the reconstruction of the shape of each segment on map view (Figure 9). Overall, each segment appears elongated along a NW/SE direction. In addition, the long axes of the concordant segments have the same average NW-SE orientations as those of the steeply dipping steps (Figure 9).

The splitting of a single sill to slightly offset segments have been observed on 3D seismic data (e.g., Schofield et al., 2012; Schmiedel et al., 2017; Magee et al., 2019), on field observations (e.g., Hutton, 2009; Galland et al., 2019; Magee et al., 2019) and produced in 3D laboratory models (Arachchige et al., 2022). Such a splitting of a sheet to distinct segments is

actually a general phenomenon associated with the emplacement of igneous sheet intrusions, including dykes (e.g., Pollard et al., 1982; Takada, 1990; Sigmundsson et al., 2015; Schmiedel et al., 2021). This splitting is expected to spontaneously occur when instabilities form at the propagating front of a sheet intrusion when the magma overpressure or influx is expected to be large (Takada, 1990).

5.2 Stratigraphic control on sill morphology

Our mapping highlights that sill segments emplaced near the stratigraphic boundary between the Gipshuken and the Kapp Starostin formations are straight and concordant, and are terminated laterally by a steeply dipping step structure (Figure 6C, Figure 7 and Figure 8). Conversely, the small outcrops of the sill segments emplaced within the Kapp Starostin Formation exhibit irregular shapes (Figure 4, Figure 8). Our data thus highlight a correlation between the intrusion morphology and the stratigraphic level of emplacement.

The boundary between the Gipshuken and the Kapp Starostin formations is marked by both (1) a thick and competent fossil-rich carbonate layer (Vøringen Member; Figure 6) and (2) a sharp lithological contrast between the evaporite-rich formation below and the clay-rich formations above. This stratigraphic level thus likely corresponds to a strong mechanical layering that may have controlled the very flat morphology of the concordant sill segments. Nevertheless, classic elastic models of dyke and sill emplacement in the layered crust predict that when a dyke reaches the base of a stiffer layer, the dyke is blocked and turns into a sill underneath the stiff layer (e.g., Rivalta et al., 2005; Gudmundsson and Philipp, 2006; Kavanagh et al., 2006). If this process was at work, we would expect the sill segments to be emplaced underneath the Vøringen Member. However, the observed straight sill segments were either emplaced a few meters below or above the Vøringen Member within softer sediments, in contradiction with the predictions of the elastic models. A similar configuration has been

observed in the Neuquén Basin, Argentina, where sills were emplaced almost systematically at the interface between an underlying stiff carbonate layer and overlaying softer organic-rich shale (Spacapan et al., 2018; Palma et al., 2024). This configuration suggests that the emplacement of the straight sill segments was governed by the rheological contrast between the underlying stiff, elastic carbonate layer and the overlaying soft, likely inelastic clay/chert deposits of the lower Kapp Starostin Formation. Further understanding requires mapping emplacement-related deformation structures in the host rock (Spacapan et al., 2017; Galland et al., 2019), which were not visible in the field.

In contrast, the more homogeneous package of the Kapp Starostin Formation may have favoured the emplacement of more irregular segments of the sill (see lower contacts of sill segments emplaced within Kapp Starostin Formation in Figure 4), similarly to large sills emplaced in the Triassic organic-rich shale in Svalbard (Senger and Galland, 2022).

5.3 Mechanics of step formation

Most steps mapped in the study area exhibit a steeply dipping sheet shape connecting the lateral edges of two sill segments emplaced at different stratigraphic levels (Figure 7 and Figure 9). Such connections have been commonly observed on 2D outcrops (Hutton, 2009; Eide et al., 2016; Stephens et al., 2021; Kjenes et al., 2022) and inferred from seismic data (Schofield et al., 2012; Köpping et al., 2022). Our field observations provide detailed constraints on the mechanism of step formation.

The steeply-dipping sheet structure of the steps differs from the structure of broken bridges between sill and dyke segments (Figure 10) (Nicholson and Pollard, 1985; Weinberger et al., 2000; Hutton, 2009; Schofield et al., 2012; Magee et al., 2019; Stephens et al., 2021; Köpping et al., 2022). Broken bridges connect overlapping intrusion tips, with a piece of host rock (a bridge) sheared in between the overlapping tips (Figure 10C). When shearing is

sufficient, the bridge breaks after bending and a channel connects the two segments. The breakage of the bridge can occur as a single channel or through brecciation of the bridge, resulting in many magmatic splays (Stephens et al., 2021; Kjenes et al., 2022). All in all, after bridge formation, the tips of the overlapping sill segments are commonly preserved beyond the broken bridge (see Figure 10C) and visible in the field.

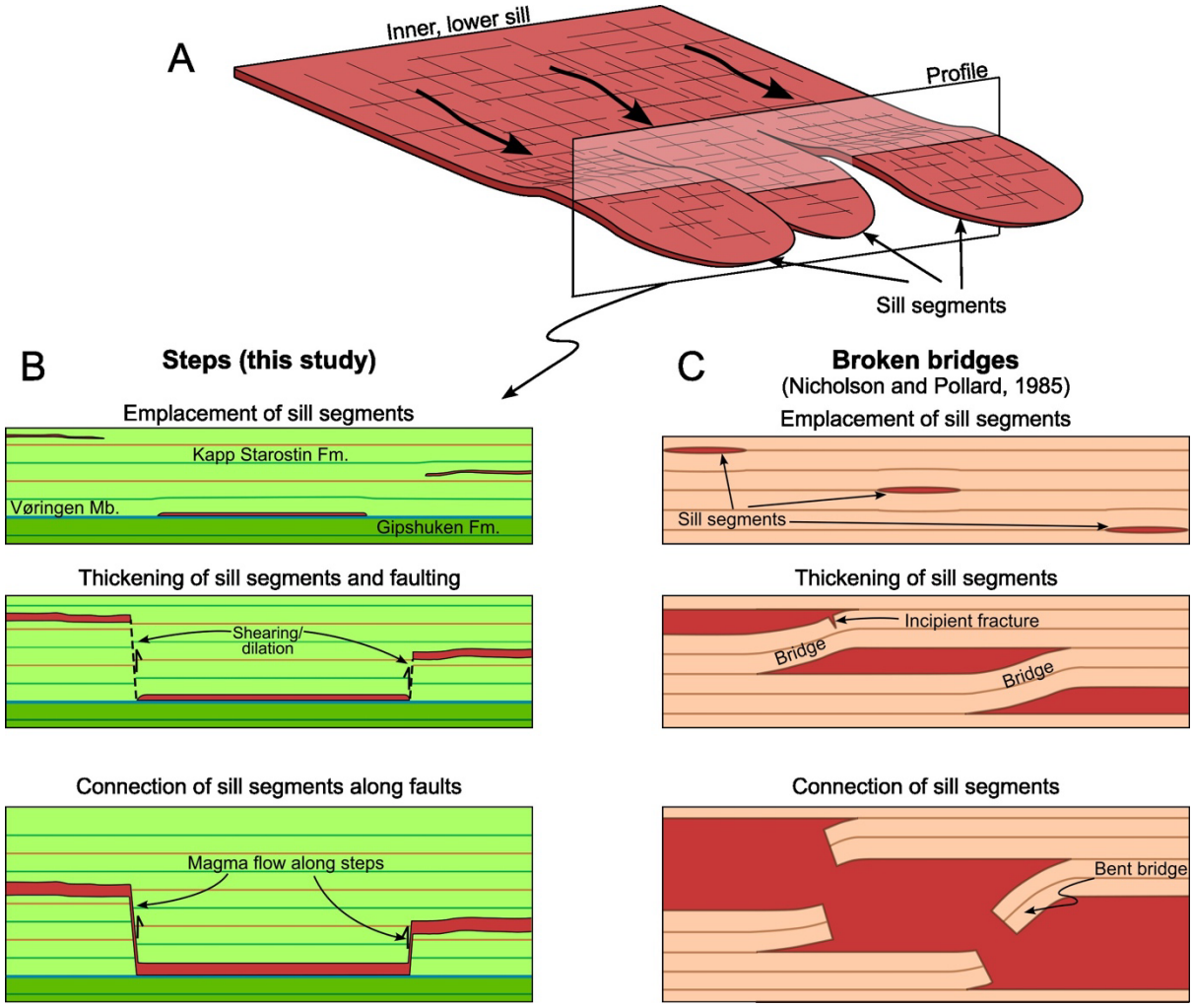

Figure 10. A. 3D block diagram drawing of the structure of the sill described in this study. Bold arrows indicate main magma flow direction from NW to SE. Transparent rectangle indicates location of cross sections of B. B. Time sequence of cross sections located in A (perpendicular to propagation direction) illustrating the formation of steps between sill segments emplaced at different stratigraphic levels. C. Time sequence of cross sections illustrating the formation of

460 broken bridges, perpendicular to the main intrusion propagation direction, as described by
461 Nicholson and Pollard (1985).
462
463 The structure of the steps described in this paper is different. There is a sharp transition
464 between the lower sill segment and the steeply dipping step, with no evidence of preserved sill
465 tip beyond the step (Figure 7) (Magee et al., 2019), suggesting that the tips of the sill segments
466 connected by the steps did not overlap. Instead, we propose the following mechanism based on
467 our field observations. When two sill segments emplaced at different stratigraphic levels inflate
468 by roof uplift, the host rock layers just above the lower sill segment lift up, whereas they are
469 below the floor of the upper sill segment and thus do not lift up (see green layer above lower
470 sill in Figure 10B). Such differential uplift leads to bending/shearing of rock layers between
471 the lower and upper sill segments. In our study area, the shearing between the sill segments
472 may be such that the host rock fails. However, because of the frictional properties of brittle
473 rocks, shearing cannot occur along a perfectly vertical plane, and a dilating component is
474 necessary to accommodate shear failure (Davis and Selvadurai, 2005; Haug et al., 2017).
475 Consequently, the steps are not expected to be vertical, but to be steeply dipping toward the
476 lower sill segment (Figure 10B). Uplift accommodated by inward dipping planes (Figure 10B)
477 kinematically requires a dilation component, which may help the magma to invade the plane
478 of the step structure.
479 The rock layers above the upper sill segments are lifted by both the inflating lower and
480 upper sill segments, therefore they are expected to not be deformed, or in a negligible manner.
481 One could argue that the steps follow pre-existing faults that affect the stratigraphy,
482 like igneous and sandstone intrusions deflected by normal faults described by Magee et al.
483 (2013) and Bureau et al. (2013), respectively. Nevertheless, if pre-existing tectonic faults
484 existed before the emplacement of the sill, they would affect the stratigraphy below and above

485 the steps, whereas our field observations show no evidence of tectonic offset of the sedimentary
486 strata below the steps. This observation thus shows that the vertical offset of the sedimentary
487 layers on both sides of the steps does nor result from tectonic faulting. Similar conclusions
488 were derived from the geological observations of Galland et al. (2019), who described intense
489 deformation of the host rock in between sill segments, but no deformation below and above.
490 Note that Figure 10B is a 2-dimensional interpretation of a 3-dimensional problem. It
491 is therefore likely that the step initiates where the sill segments split from the common feeder
492 sill (Figure 10A), and propagates laterally with the propagating segments.
493

494 ## 5.4 Magma flow direction

495 On a regional scale, it is still not clear how magma was emplaced in Svalbard. In particular,
496 the interaction of magma with pre-existing weakness zones like the Billefjorden Fault Zone
497 remains unclear (Senger and Galland, 2022). Similarly, regional magma emplacement
498 directions and mechanisms related to HALIP pulsing are unknown. The result of our mapping
499 may shed light on the magma flow direction at work during the emplacement of the studied
500 sill.
501 The mapped subvertical steps exhibit a NW-SE to NNW-SSE preferred orientation
502 (Figure 7A). These steps have been interpreted in the literature as markers of magma flow
503 direction parallel to the step orientation (Thomson, 2007; Hutton, 2009; Magee et al., 2019;
504 Köpping et al., 2022). We infer from the steps that the magma likely flowed either from the
505 NW-NNW to the SE-SSE, or *vice-versa*.
506 Sill emplacement models predict that sills thin from their feeders toward their tips
507 (Pollard and Johnson, 1973; Kerr and Pollard, 1998; Galland and Scheibert, 2013). The
508 systematic thinning of the sill from the NW to the SE thus suggests that the magma source was
509 located northwest of the study area, and that the magma flowed toward the SE-SSE. A last

point of consideration is the depth of the sill segments. The deepest segment mapped in the study area is exposed at Peak 729, i.e. in the NW sector of the study area (Figure 3). This again suggests that the sill is fed from the NW, where the feeder is expected to bring the magma from depth.

The individual segments of the mapped sill were likely fed from a common feeder structure (Figure 10). The sill imaged on 3D seismic data in Figure 1 exhibits a deep basal sill connected, and likely feeding, sill segments emplaced at different stratigraphic levels (Kjøll et al., 2024). A similar structure is expected for the studied sill, suggesting that a large basal sill may have fed the mapped intrusion from northwest. Our field mapping showed no evidence that the feeder of the studied sill could be related to structural lineaments, such as the Blomesletta fault.

5.5 Volume estimate of the exposed sill

In this section we provide a rough volume estimate of the studied sill. By estimating the area highlighted in Figure 9 on Google Earth, and multiplying this area (~70 km^2) by the average thickness we calculated from our thickness measurements (65.7 m), a simple volume estimate calculation of the mapped sill yields ~4.6 km^3. If we include Blomesletta in the measured area (see section 5.1), this yields an estimated sill volume of ~6.7 km^3. Finally, on the western flank of Ekmanfjorden at the summit of Kolosseum, a dolerite sill was emplaced within the Kapp Starostin Formation (Dallmann, 2015), suggesting that it is part of the sill described in this study. If we extend the area of the sill to Kolosseum, this yields an estimated sill volume of ~11.4 km^3. It is likely that the studied sill extends far beyond the study area, as large sill segments of similar thickness are observed on the other sides of Ekmanfjorden and Dicksonfjorden (Dallmann, 2015; Senger and Galland, 2022; Sartell et al., in press). Thus, this estimate is likely an underestimate of the actual intrusion volume.

Yet, such volume is significantly larger than the very large majority of basaltic lava eruptions during the Holocene. As a matter of comparison, the infamous 1783-1784 Laki and 934 Eldgjá eruptions, Iceland, erupted volumes of ~14 km^3 and ~19 km^3, respectively (Thordarson and Self, 1993). The volume of the studied sill has a similar order of magnitude as those of Laki and Eldgjá eruptions, which are considered to be the two largest basaltic eruptions of historical times. In addition, the estimated volume of the studied sill is slightly smaller than that of the Golden Valley Sill, South Africa, the thickness and area of which are ~100 m and ~200 km^2, respectively, so the estimated volume being ~20 km^3 (Galerne et al., 2010; Galerne et al., 2011). Thus, the volume of the mapped sill is of the same order of magnitude as those of (1) sills formed in a Large Igneous Province and (2) unusually large basaltic eruptions. The studied sill thus resulted from an emplacement event of significant magnitude, in agreement with the HALIP magmatic context.

6 Conclusions

This study describes the results of 3-dimensional geological mapping of a large Early Cretaceous dolerite sill exposed in steep, near-vertical cliffs using a combination of digital outcrop modelling and field mapping. The main results of this study are the following.

- The sill is made of distinct segments emplaced at different stratigraphic levels of the host rock stratigraphy.
- The sills segments emplaced near a strong lithological boundary are straight and very concordant. Conversely, the segments emplaced within more homogeneous formations exhibit more complex, locally discordant shapes.

- The sills segments emplaced at distinct stratigraphic levels are connected by steeply dipping steps, which formed through shearing/dilation between the tips of the sill segments.
- The preferred NW-SE orientation of the steps and the thinning of the sill towards the SE suggests a propagation direction of the magma towards the SE.
- The sill volume estimate between 4.6 and 11.4 km^3 suggests an emplacement event of large significance, in agreement with the High Arctic Large Igneous Province setting.

In summary, our study shows how 3-dimensional knowledge of igneous intrusions is key for revealing their emplacement mechanisms.

Acknowledgements

Fieldwork was mostly funded through Arctic Field Grants (AFGs; Research in Svalbard ID 11397, Norwegian Research Council project nr. 310709; Research in Svalbard ID 11619, Norwegian Research Council project nr. 322464) plus additional funding for fieldwork from NOR-R-AM2, Norwegian Research Council project nr. 309477, ARCEx, Norwegian Research Council project nr 228107 and UArctic. The fieldwork benefited from logistical support of the UArctic (drones), Czech Arctic Research Station/Clione and UNIS logistics, NFR (SSG project). Schlumberger and Cegal provided academic licences for Petrel and Blueback toolbox, respectively. Nil Rodes processed some of the drone images. Field expeditions involved field assistants (From the 2020 expedition: Peter Betlem, Marjolein Gevers, Tereza Mosočiová). HJK was funded by Aker BP through the project “80-40 Palaeocene”. AMRS's PhD position was funded by the University of Helsinki. RKH's PhD position was funded by Norwegian Centre for Integrated Earth Science Education - iEarth, The University Centre in Svalbard, and

the Norwegian Ministry of Education. We thank Dr. Craig Magee and Prof. Sandy Cruden for their very constructive reviews and Editor Prof. Atle Rotevatn for handling the manuscript.

7 References

Aarnes, I., Svensen, H., Connolly, J.A.D., Podladchikov, Y.Y., 2010. How contact metamorphism can trigger global climate changes: Modeling gas generation around igneous sills in sedimentary basins. Geochimica et Cosmochimica Acta 74, 7179-7195, doi: 10.1016/j.gca.2010.09.011.

Ahlborn, M., Stemmerik, L., 2015. Depositional evolution of the Upper Carboniferous – Lower Permian Wordiekammen carbonate platform, Nordfjorden High, central Spitsbergen, Arctic Norway. Norwegian Journal of Geology 95, 91—126, doi: http://dx.doi.org/10.17850/njg95-1-03.

Arachchige, U.N., Cruden, A.R., Weinberg, R.F., Slim, A., Köpping, J., 2022. Saucers, Fingers, and Lobes: New Insights on Sill Emplacement From Scaled Laboratory Experiments. J. Geophys. Res. 127, e2022JB024421, doi: https://doi.org/10.1029/2022JB024421.

Bælum, K., Braathen, A., 2012. Along-strike changes in fault array and rift basin geometry of the Carboniferous Billefjorden Trough, Svalbard, Norway. Tectonophysics 546-547, 38-55, doi: https://doi.org/10.1016/j.tecto.2012.04.009.

Bergh, S.G., Braathen, A., Andresen, A., 1997. Interaction of basement-involved and thin-skinned tectonism in the Tertiary fold-thrust belt of central Spitsbergen, Svalbard. American Association of Petroleum Geologists Bulletin 81, 637-661.

Betlem, P., Rodés, N., Birchall, T., Dahlin, A., Smyrak-Sikora, A., Senger, K., 2023. Svalbox Digital Model Database: A geoscientific window into the High Arctic. Geosphere 19, 1640-1666, doi: 10.1130/GES02606.1.

Blinova, M., Faleide, J.I., Gabrielsen, R.H., Mjelde, R., 2013. Analysis of structural trends of sub-sea-floor strata in the Isfjorden area of the West Spitsbergen Fold-and-Thrust Belt based on multichannel seismic data. J. Geol. Soc. 170, 657-668, doi: 10.1144/jgs2012-109.

Blomeier, D., Dustira, A.M., Forke, H., Scheibner, C., 2013. Facies analysis and depositional environments of a storm-dominated, temperate to cold, mixed siliceous-carbonate ramp: the Permian Kapp Starostin Formation in NE Svalbard. Norwegian Journal of Geology 93, 75-93.

Blomeier, D., Scheibner, C., Forke, H., 2009. Facies arrangement and cyclostratigraphic architecture of a shallow-marine, warm-water carbonate platform: the Late Carboniferous Ny Friesland Platform in eastern Spitsbergen (Pyefjellet Beds, Wordiekammen Formation, Gipsdalen Group). Facies 55, 291-324.

Bonali, F.L., Tibaldi, A., Corti, N., Fallati, L., Russo, E., 2020. Reconstruction of Late Pleistocene-Holocene Deformation through Massive Data Collection at Krafla Rift (NE Iceland) Owing to Drone-Based Structure-from-Motion Photogrammetry, Applied Sciences, doi: 10.3390/app10196759.

Bond, D.P.G., Blomeier, D.P.G., Dustira, A.M., Wignall, P.B., Collins, D., Goode, T., Groen, R.D., Buggisch, W., Grasby, S.E., 2018. Sequence stratigraphy, basin morphology and sea-level history for the Permian Kapp Starostin Formation of Svalbard, Norway. Geological Magazine 155, 1023-1039, doi: 10.1017/S0016756816001126.

Braathen, A., Osmundsen, P.T., Maher, H., Ganerød, M., 2018. The Keisarhjelmen detachment records Silurian–Devonian extensional collapse in Northern Svalbard. Terra Nova 30, 34-39.

Buckley, S.J., Howell, J.A., Naumann, N., Lewis, C., Chmielewska, M., Ringdal, K., Vanbiervliet, J., Tong, B., Mulelid-Tynes, O.S., Foster, D., Maxwell, G., Pugsley, J., 2022. V3Geo: a cloud-based repository for virtual 3D models in geoscience. Geosci. Commun. 5, 67-82, doi: 10.5194/gc-5-67-2022.

628 Buckley, S.J., Ringdal, K., Naumann, N., Dolva, B., Kurz, T.H., Howell, J.A., Dewez, T.J.B.,
629 2019. LIME: Software for 3-D visualization, interpretation, and communication of virtual
630 geoscience models. Geosphere 15, 222-235, doi: 10.1130/GES02002.1.

631 Bureau, D., Mourgues, R., Cartwright, J., Foschi, M., Abdelmalak, M.M., 2013.
632 Characterisation of interactions between a pre-existing polygonal fault system and sandstone
633 intrusions and the determination of paleo-stresses in the Faroe-Shetland basin. J. Struct. Geol.
634 46, 186-199, doi: http://dx.doi.org/10.1016/j.jsg.2012.09.003.

635 Chevallier, L., Gibson, L.A., HNhleko, L.O., Woodford, A.C., Nomquphu, W., Kippie, I.,
636 2004. Hydrogeology of fractured-rock aquifers and related ecosystems within the Qoqodala
637 dolerite ring and sill complex, Great Kei catchment, Eastern Cape, Water Res. Com., S. Afr.
638 Water Research Commission, p. 127.

639 Chevallier, L., Goedhart, M., Woodford, A., 2001. The influence of dolerite sill and ring
640 complexes on the occurrence of grounwater in the Karoo fractured aquifers: a morpho-tectonic
641 approach, Water Res. Com., S. Afr., p. 143.

642 Courtillot, V.E., Renne, P.R., 2003. On the ages of flood basalt events. Comptes Rendus
643 Geoscience 335, 113-140, doi: https://doi.org/10.1016/S1631-0713(03)00006-3.

644 Crameri, F., Shephard, G.E., Heron, P.J., 2020. The misuse of colour in science
645 communication. Nature Communications 11, 5444, doi: 10.1038/s41467-020-19160-7.

646 Dallmann, W., 1999. Lithostratigraphic lexicon of Svalbard. Norsk Polarinstitutt, p. 318.

647 Author, 2014. Geological map of Svalbard (1:750000), doi:
648 doi.org/10.21334/npolar.2014.09dbe7b2.

649 Dallmann, W.K., 2015. Geoscience Atlas of Svalbard, Report Series. Norgegian Polar Institute,
650 Tromsø, p. 292.

651 Davis, R.O., Selvadurai, A.P.S., 2005. Plasticity and Geomechanics. Cambridge, UK,
652 Cambridge University Press.

653 de Miranda, F.S., Vettorazzi, A.L., Cunha, P.R.d.C., Aragão, F.B., Michelon, D., Caldeira,
654 J.L., Porsche, E., Martins, C., Ribeiro, R.B., Vilela, A.F., Corrêa, J.R., Silveira, L.S., Andreola,
655 K., 2018. Atypical igneous-sedimentary petroleum systems of the Parnaíba Basin, Brazil:
656 seismic, well logs and cores. Geol. Soc. London. Spec. Pub. 472, 341, doi: 10.1144/SP472.15.

657 Eide, C.H., Schofield, N., Jerram, D.A., Howell, J.A., 2016. Basin-scale architecture of deeply
658 emplaced sill complexes: Jameson Land, East Greenland. J. Geol. Soc. 174, 23-40, doi:
659 10.1144/jgs2016-018.

660 Einsele, G., Gieskes, J.M., Curray, J., Moore, D.M., Aguayo, E., Aubry, M.-P., Fornari, D.,
661 Guerrero, J., Kastner, M., Kelts, K., Lyle, M., Matoba, Y., Molina-Cruz, A., Niemitz, J., Rueda,
662 J., Saunders, A., Schrader, H., Simoneit, B., Vacquier, V., 1980. Intrusion of basaltic sills into
663 highly porous sediments, and resulting hydrothermal activity. Nature 283, 441-445, doi:
664 10.1038/283441a0.

665 Galerne, C.Y., Galland, O., Neumann, E.R., Planke, S., 2011. 3D relationships between sills
666 and their feeders: evidence from the Golden Valley Sill Complex (Karoo Basin) and
667 experimental modelling. J. Volcanol. Geotherm. Res. 202, 189-199, doi:
668 10.1016/j.jvolgeores.2011.02.006.

669 Galerne, C.Y., Hasenclever, J., 2019. Distinct Degassing Pulses During Magma Invasion in
670 the Stratified Karoo Basin—New Insights From Hydrothermal Fluid Flow Modeling. G3 20,
671 2955-2984, doi: https://doi.org/10.1029/2018GC008120.

672 Galerne, C.Y., Neumann, E.R., Aarnes, I., Planke, S., 2010. Magmatic differentiation processes
673 in saucer-shaped sills: Evidence from the Golden Valley Sill in the Karoo Basin, South Africa.
674 Geosphere 6, 163-188, doi: 10.1130/ges00500.1.

675 Galland, O., Bertelsen, H.S., Eide, C.H., Guldstrand, F., Haug, Ø.T., Leanza, H.A., Mair, K.,
676 Palma, O., Planke, S., Rabbel, O., Rogers, B.D., Schmiedel, T., Souche, A., Spacapan, J.B.,
677 2018. Storage and transport of magma in the layered crust-Formation of sills and related flat-
678 lying intrusions, in: Burchardt, S. (Ed.), Volcanic and Igneous Plumbing Systems. Elsevier, pp.
679 111-136, doi: http://dx.doi.10.1016/B978-0-12-809749-6.00005-4.

680 Galland, O., Scheibert, J., 2013. Analytical model of surface uplift above axisymmetric flat-
681 lying magma intrusions: Implications for sill emplacement and geodesy. J. Volcanol.
682 Geotherm. Res. 253, 114-130, doi: http://dx.doi.org/10.1016/j.jvolgeores.2012.12.006.

683 Galland, O., Spacapan, J.B., Rabbel, O., Mair, K., Soto, F.G., Eiken, T., Schiuma, M., Leanza,
684 H.A., 2019. Structure, emplacement mechanism and magma-flow significance of igneous
685 fingers – Implications for sill emplacement in sedimentary basins. J. Struct. Geol. 124, 120–
686 135, doi: https://doi.org/10.1016/j.jsg.2019.04.013.

687 Gudmundsson, A., Philipp, S.L., 2006. How local stress fields prevent volcanic eruptions. J.
688 Volcanol. Geotherm. Res. 158, 257-268.

689 Hansen, D.M., Cartwright, J.A., 2006. Saucer-shaped sill with lobate morphology revealed by
690 3D seismic data: implications for resolving a shallow-level sill emplacement mechanism. J.
691 Geol. Soc. London 163, 509-523.

692 Haug, Ø.T., Galland, O., Souloumiac, P., Souche, A., Guldstrand, F., Schmiedel, T., 2017.
693 Inelastic damage as a mechanical precursor for the emplacement of saucer-shaped intrusions.
694 Geology 45, 1099-1102, doi: 10.1130/G39361.1.

695 Author, 2024. Svalbox-DOM_2021-0058, doi: https://doi.org/10.5281/zenodo.13842312.

696 Hutton, D.H.W., 2009. Insights into magmatism in volcanic margins: bridge structures and a
697 new mechanism of basic sill emplacement, Theron Mountains, Antarctica. Petroleum
698 Geoscience 15, 269-278, doi: 10.1144/1354-079309-841.

699 Ineson, J.R., Hovikoski, J., Sheldon, E., Piasecki, S., Alsen, P., Fyhn, M.B., Bjerager, M.,
700 Dybkjær, K., Guarnieri, P., Lauridsen, B.W., 2021. Regional impact of Early Cretaceous
701 tectono-magmatic uplift in the Arctic: Implications of new data from eastern North Greenland.
702 Terra Nova 33, 284-292.

703 Author, 2014a. Kartdata Svalbard 1:100 000 (S100 Kartdata, NP_S100_SHP), doi:
704 https://doi.org/10.21334/npolar.2014.645336c7.

705 Author, 2014b. Terrengmodell Svalbard (S0 Terrengmodell, NP_S0_DTM20), doi:
706 https://doi.org/10.21334/npolar.2014.dce53a47.

707 Author, 2016. Geological map of Svalbard (1_250 000, G250_Geology), doi:
708 https://doi.org/10.21334/npolar.2016.616f7504.

709 Iyer, K., Schmid, D.W., Planke, S., Millett, J., 2017. Modelling hydrothermal venting in
710 volcanic sedimentary basins: Impact on hydrocarbon maturation and paleoclimate. Earth
711 Planet. Sci. Lett. 467, 30-42, doi: https://doi.org/10.1016/j.epsl.2017.03.023.

712 Jakobsson, M., Mayer, L., Coakley, B., Dowdeswell, J.A., Forbes, S., Fridman, B., Hodnesdal,
713 H., Noormets, R., Pedersen, R., Rebesco, M., Schenke, H.W., Zarayskaya, Y., Accettella, D.,
714 Armstrong, A., Anderson, R.M., Bienhoff, P., Camerlenghi, A., Church, I., Edwards, M.,
715 Gardner, J.V., Hall, J.K., Hell, B., Hestvik, O., Kristoffersen, Y., Marcussen, C., Mohammad,
716 R., Mosher, D., Nghiem, S.V., Pedrosa, M.T., Travaglini, P.G., Weatherall, P., 2012. The
717 International Bathymetric Chart of the Arctic Ocean (IBCAO) Version 3.0. Geophys. Res. Lett.
718 39, doi: https://doi.org/10.1029/2012GL052219.

719 Kavanagh, J.L., Menand, T., Sparks, R.S.J., 2006. An experimental investigation of sill
720 formation and propagation in layered elastic media. Earth Planet. Sci. Lett. 245, 799-813.

721 Kerr, A.D., Pollard, D.D., 1998. Toward more realistic formulations for the analysis of
722 laccoliths. J. Struct. Geol. 20, 1783-1793.

723 Kjenes, M., Eide, C.H., Schofield, N., Chedburn, L., 2022. Alkaline sill intrusions in
724 sedimentary basins: emplacement of the Mussentuchit Wash Sill in San Rafael Swell, Utah. J.
725 Geol. Soc. 0, jgs2021-2139, doi: 10.1144/jgs2021-139.

726 Kjøll, H.J., Midtkandal, I., Planke, S., Millett, J., Manton, B., Anderskouv, K., 2024. The
727 interplay between siliciclastic and carbonate depositional systems: Maastrichtian to Danian
728 basin-floor sediments of the mid-Norwegian Møre Basin. Basin Res. 36, e12827, doi:
729 https://doi.org/10.1111/bre.12827.

730 Köpping, J., Magee, C., Cruden, A.R., Jackson, C.A.L., Norcliffe, J.R., 2022. The building
731 blocks of igneous sheet intrusions: Insights from 3-D seismic reflection data. Geosphere 18,
732 156-182, doi: 10.1130/GES02390.1.

733 Krajewski, K.P., 2013. Organic matter–apatite–pyrite relationships in the Botneheia Formation
734 (Middle Triassic) of eastern Svalbard: Relevance to the formation of petroleum source rocks
735 in the NW Barents Sea shelf. Marine and Petroleum Geology 45, 69-105, doi:
736 http://dx.doi.org/10.1016/j.marpetgeo.2013.04.016.

737 Lasabuda, A.P.E., Johansen, N.S., Laberg, J.S., Faleide, J.I., Senger, K., Rydningen, T.A.,
738 Patton, H., Knutsen, S.-M., Hanssen, A., 2021. Cenozoic uplift and erosion of the Norwegian
739 Barents Shelf – A review. Earth-Sci. Rev. 217, 103609, doi:
740 https://doi.org/10.1016/j.earscirev.2021.103609.

741 Lombardo, E.F., Galland, O., Yagupsky, D., Jerram, D.A., 2024. Characterization of a
742 structural trap associated with an intrusive complex: the El Trapial Oil Field, Neuquén basin,
743 Argentina, in: Kilhams, B., Watson, D., Holford, S. (Eds.), Geol. Soc. London. Spec. Pub.
744 Geological Society, London, Special Publications, doi: 10.1144/SP547-2023-98.

745 Magee, C., Jackson, C.A.-L., Schofield, N., 2013. The influence of normal fault geometry on
746 igneous sill emplacement and morphology. Geology 41, 407-410, doi: 10.1130/g33824.1.

747 Magee, C., Muirhead, J.D., Karvelas, A., Holford, S.P., Jackson, C.A.L., Bastow, I.D.,
748 Schofield, N., Stevenson, C.T.E., McLean, C., McCarthy, W., Shtukert, O., 2016. Lateral
749 magma flow in mafic sill complexes. Geosphere 12, 809-841, doi: 10.1130/ges01256.1.

750 Magee, C., Muirhead, J.D., Schofield, N., Walker, R.J., Galland, O., Holford, S., Spacapan,
751 J.B., Jackson, C.A.L., McCarthy, W., 2019. Structural signatures of igneous sheet intrusion
752 propagation. J. Struct. Geol. 125, 148-154, doi: https://doi.org/10.1016/j.jsg.2018.07.010.

753 Maher, J.H.D., 2001. Manifestations of the Cretaceous High Arctic Large Igneous Province in
754 Svalbard. The Journal of Geology 109, 91-104, doi: 10.1086/317960.

755 Mark, N.J., Schofield, N., Pugliese, S., Watson, D., Holford, S., Muirhead, D., Brown, R.,
756 Healy, D., 2018. Igneous intrusions in the Faroe Shetland basin and their implications for
757 hydrocarbon exploration; new insights from well and seismic data. Mar. Pet. Geol. 92, 733-
758 753, doi: https://doi.org/10.1016/j.marpetgeo.2017.12.005.

759 Nicholson, R., Pollard, D.D., 1985. Dilation and linkage of echelon cracks. J. Struct. Geol. 7,
760 583-590, doi: https://doi.org/10.1016/0191-8141(85)90030-6.

761 Olaussen, S., Grundvåg, S.-A., Senger, K., Anell, I., Betlem, P., Birchall, T., Braathen, A.,
762 Dallmann, W.K., Jochmann, M., Johannessen, E.P., Lord, G., Mørk, A., Osmundsen, P.T.,
763 Smyrak-Sikora, A., Stemmerik, L., 2025. Svalbard Composite Tectono-Sedimentary Element,
764 Barents Sea. Geological Society, London, Memoirs 57, M57-2021-2036, doi: 10.1144/M57-
765 2021-36.

766 Palma, J.O., Rabbel, O., Spacapan, J.B., Ruiz, R., Galland, O., 2024. The Cara Cura intrusive
767 complex, Neuquén Basin, Argentina: a field analogue of a whole igneous petroleum system,
768 in: Kilhams, B., Watson, D., Holford, S. (Eds.), The Impacts of Igneous Systems on
769 Sedimentary Basins and Their Energy Resources. Geological Society, London, Special
770 Publications, doi: https://doi.org/10.1144/SP547-2023-119.

771 Piepjohn, K., 2000. The Svalbardian-Ellesmerian deformation of the Old Red Sandstone and
772 the pre-Devonian basement in NW Spitsbergen (Svalbard). Geological Society, London,
773 Special Publications 180, 585-601.

774 Planke, S., Rasmussen, T., Rey, S.S., Myklebust, R., 2005. Seismic characteristics and
775 distribution of volcanic intrusions and hydrothermal vent complexes in the Vøring and Møre
776 basins, in: Doré, A.G., Vining, B.A. (Eds.), Petroleum Geology: North-West Europe and
777 Global Perspectives—Proceedings of the 6th Petroleum Geology Conference. Geological
778 Society, London, London, pp. 833-844.

779 Pollard, D.D., Johnson, A.M., 1973. Mechanics of growth of some laccolithic intrusions in the
780 Henry Mountains, Utah, II. Bending and failure of overburden layers and sill formation.
781 Tectonophysics 18, 311-354.

782 Pollard, D.D., Segall, P., Delaney, P.T., 1982. Formation and interpretation of dilatant echelon
783 cracks. Geol. Soc. Am. Bull. 93, 1291-1303.

784 Polteau, S., Ferré, E.C., Planke, S., Neumann, E.-R., Chevallier, L., 2008. How are saucer-
785 shaped sills emplaced? Constraints from the Golden Valley Sill, South Africa. J. Geophys. Res.
786 113, doi: 10.1029/2008JB005620.

787 Polteau, S., Hendriks, B.W.H., Planke, S., Ganerød, M., Corfu, F., Faleide, J.I., Midtkandal, I.,
788 Svensen, H.S., Myklebust, R., 2016. The Early Cretaceous Barents Sea Sill Complex:
789 Distribution, 40Ar/39Ar geochronology, and implications for carbon gas formation.
790 Palaeogeography, Palaeoclimatology, Palaeoecology 441, 83-95, doi:
791 https://doi.org/10.1016/j.palaeo.2015.07.007.

792 Rabbel, O., Galland, O., Mair, K., Lecomte, I., Senger, K., Spacapan, J.B., Manceda, R., 2018.
793 From field analogues to realistic seismic modelling: a case study of an oil-producing andesitic
794 sill complex in the Neuquén Basin, Argentina. J. Geol. Soc., doi: 10.1144/jgs2017-116.

795 Rabbel, O., Palma, J.O., Mair, K., Galland, O., Spacapan, J.B., Senger, K., 2021. Fracture
796 networks in shale-hosted igneous intrusions: Processes, distribution and implications for
797 igneous petroleum systems. J. Struct. Geol. 150, 104403, doi:
798 https://doi.org/10.1016/j.jsg.2021.104403.

799 Rivalta, E., Böttinger, M., Dahm, T., 2005. Buoyancy-driven fracture ascent: Experiments in
800 layered gelatine. J. Volcanol. Geotherm. Res. 144, 273-285.

801 Sartell, A.M.R., 2021. The igneous complex of Ekmanfjorden, Svalbard: an integrated field,
802 petrological and geochemical study, Department of Geology. Lund University, Lund, Sweden.

803 Sartell, A.M.R., Söderlund, U., Senger, K., Kjøll, H.J., Galland, O., in press. A Review of the
804 Spatiotemporal Evolution of the High Arctic Large Igneous Province, and a New U-Pb Age of
805 a Mafic Sill Complex on Svalbard. G3.

806 Schmiedel, T., Burchardt, S., Mattsson, T., Guldstrand, F., Galland, O., Palma, J.O., Skogby,
807 H., 2021. Emplacement and Segment Geometry of Large, High-Viscosity Magmatic Sheets.
808 Minerals 11, doi: 10.3390/min11101113.

809 Schmiedel, T., Kjoberg, S., Planke, S., Magee, C., Galland, O., Schofield, N., Jackson, C.A.-
810 L., Jerram, D.A., 2017. Mechanisms of overburden deformation associated with the
811 emplacement of the Tulipan sill, mid-Norwegian margin. Interpretation 5, SK23-SK38, doi:
812 10.1190/int-2016-0155.1.

813 Schofield, N., Heaton, L., Holford, S.P., Archer, S.G., Jackson, C.A.L., Jolley, D.W., 2012.
814 Seismic imaging of "broken bridges": linking seismic to outcrop-scale investigations of
815 intrusive magma lobes. J. Geol. Soc. 169, 421-426, doi: 10.1144/0016-76492011-150.

816 Senger, K., Betlem, P., Birchall, T., Buckley, S.J., Coakley, B., Eide, C.H., Flaig, P.P., Forien,
817 M., Galland, O., Gonzaga, L., Jensen, M., Kurz, T., Lecomte, I., Mair, K., Malm, R.H.,
818 Mulrooney, M., Naumann, N., Nordmo, I., Nolde, N., Ogata, K., Rabbel, O., Schaaf, N.W.,
819 Smyrak-Sikora, A., 2020. Using digital outcrops to make the high Arctic more accessible

through the Svalbox database. Journal of Geoscience Education, 1-15, doi: 10.1080/10899995.2020.1813865.

Senger, K., Galland, O., 2022. Stratigraphic and Spatial Extent of HALIP Magmatism in Central Spitsbergen. G3 23, e2021GC010300, doi: https://doi.org/10.1029/2021GC010300.

Senger, K., Millett, J., Planke, S., Ogata, K., Eide, C.H., Festøy, M., Galland, O., Jerram, D.A., 2017. Effects of igneous intrusions on the petroleum system: a review. First Break 35, 47-56, doi: 10.3997/1365-2397.2017011.

Senger, K., Planke, S., Polteau, S., Ogata, K., Svensen, H., 2014a. Sill emplacement and contact metamorphism in a siliciclastic reservoir on Svalbard, Arctic Norway. Norwegian Journal of Geology 94, 155-169.

Senger, K., Roy, S., Braathen, A., Buckley, S.J., Bælum, K., Gernigon, L., Mjelde, R., Noormets, R., Ogata, K., Olaussen, S., Planke, S., Ruud, B.O., Tveranger, J., 2013. Geometries of doleritic intrusions in central Spitsbergen, Svalbard: an integrated study of an onshore-offshore magmatic province with implications for CO2 sequestration. Norwegian Journal of Geology 93, 143-166.

Senger, K., Tveranger, J., Ogata, K., Braathen, A., Planke, S., 2014b. Late Mesozoic magmatism in Svalbard: A review. Earth-Sci. Rev. 139, 123-144, doi: 10.1016/j.earscirev.2014.09.002.

Sigmundsson, F., Hooper, A., Hreinsdóttir, S., Vogfjörd, K.S., Ófeigsson, B.G., Heimisson, E.R., Dumont, S., Parks, M., Spaans, K., Gudmundsson, G.B., Drouin, V., Árnadóttir, T., Jónsdóttir, K., Gudmundsson, M.T., Högnadóttir, T., Fridriksdóttir, H.M., Hensch, M., Einarsson, P., Magnússon, E., Samsonov, S., Brandsdóttir, B., White, R.S., Ágústsdóttir, T., Greenfield, T., Green, R.G., Hjartardóttir, Á.R., Pedersen, R., Bennett, R.A., Geirsson, H., La Femina, P.C., Björnsson, H., Pálsson, F., Sturkell, E., Bean, C.J., Möllhoff, M., Braiden, A.K., Eibl, E.P.S., 2015. Segmented lateral dyke growth in a rifting event at Bárðarbunga volcanic system, Iceland. Nature 517, 191, doi: 10.1038/nature14111 https://www.nature.com/articles/nature14111#supplementary-information.

847 Smelror, M., Larssen, G.B., 2016. Are there Upper Cretaceous sedimentary rocks preserved on
848 Sørkapp land, Svalbard? Norwegian Journal of Geology 96, 147-158, doi: 10.7850/njg96-2-
849 05.

850 Sorento, T., Olaussen, S., Stemmerik, L., 2020. Controls on deposition of shallow marine
851 carbonates and evaporites – lower Permian Gipshuken Formation, central Spitsbergen, Arctic
852 Norway. Sedimentology 67, 207-238, doi: https://doi.org/10.1111/sed.12640.

853 Spacapan, J.B., D'Odorico, A., Palma, O., Galland, O., Rojas Vera, E., Ruiz, R., Leanza, H.A.,
854 Medialdea, A., Manceda, R., 2020a. Igneous petroleum systems in the Malargüe fold and thrust
855 belt, Río Grande Valley area, Neuquén Basin, Argentina. Mar. Pet. Geol. 111, 309-331, doi:
856 https://doi.org/10.1016/j.marpetgeo.2019.08.038.

857 Spacapan, J.B., Galland, O., Leanza, H.A., Planke, S., 2017. Igneous sill and finger
858 emplacement mechanism in shale-dominated formations: a field study at Cuesta del Chihuido,
859 Neuquén Basin, Argentina. J. Geol. Soc. 174, 422-433, doi: 10.1144/jgs2016-056.

860 Spacapan, J.B., Palma, O., Galland, O., Manceda, R., Rocha, E., D'Odorico, A., Leanza, H.A.,
861 2018. Thermal impact of igneous sill complexes on organic-rich formations and the generation
862 of a petroleum system: case study in the Neuquén Basin, Argentina. Mar. Pet. Geol. 91, 519-
863 531, doi: https://doi.org/10.1016/j.marpetgeo.2018.01.018.

864 Spacapan, J.B., Ruiz, R., Manceda, R., D'Odorico, A., Rocha, E., Rojas Vera, E., Medialdea,
865 A., Cattaneo, D., Palma, J.O., Leanza, H.A., Galland, O., 2020b. Oil Production from a Sill
866 Complex Within the Vaca Muerta Formation, in: Minisini, D., Fantín, M., Lanusse Noguera,
867 I., Leanza, H.A. (Eds.), Integrated geology of unconventionals: The case of the Vaca Muerta
868 Play, Argentina. The American Association of Petroleum Geologists, Tulsa, Ohklahoma USA,
869 pp. 529-554, doi: 10.1306/13682240M1203844.

870 Steel, R.J., Worsley, D., 1984. Svalbard's post-Caledonian strata - an atlas of sedimentational
871 patterns and paleogeographic evolution, in: Spencer, A.M. (Ed.), Petroleum Geology of the
872 North European Margin. Graham & Trotman, London, pp. 109-135.

873 Stephens, T.L., Walker, R.J., Healy, D., Bubeck, A., 2021. Segment tip geometry of sheet
874 intrusions, II: Field observations of tip geometries and a model for evolving emplacement
875 mechanisms. Volcanica 4, 203 - 225, doi: 10.30909/vol.04.02.203225.

876 Svensen, H., Planke, S., Malthe-Sorenssen, A., Jamtvelt, B., Myklebust, R., Eldem, T.R., Rey,
877 S.S., 2004. Release of methane from a volcanic basin as a mechanism for initial Eocene global
878 warming. Nature 429, 542-545.

879 Svensen, H., Planke, S., Polozov, A.G., Schmidbauer, N., Corfu, F., Podladchikov, Y.Y.,
880 Jamtveit, B., 2009. Siberian gas venting and the end-Permian environmental crisis. Earth
881 Planet. Sci. Lett. 277, 490-500, doi: http://dx.doi.org/10.1016/j.epsl.2008.11.015.

882 Takada, A., 1990. Experimental study on propagation of liquid-filled crack in gelatin: shape
883 and velocity in hydrostatic stress condition. J. Geophys. Res. 95, 8471-8481.

884 Thomson, K., 2007. Determining magma flow in sills, dykes and laccoliths and their
885 implications for sill emplacement mechanisms. Bull. Volcanol. 70, 183-201.

886 Thomson, K., Hutton, D., 2004. Geometry and growth of sill complexes: insights using 3D
887 seismic from the North Rockall Trough. Bull. Volcanol. 66, 364-375.

888 Thomson, K., Schofield, N., 2008. Lithological and structural controls on the emplacement and
889 morphology of sills in sedimentary basins, in: Thomson, K., Petford, N. (Eds.), Structure and
890 Emplacement of High-Level Magmatic Systems. Geological Society, London, Special
891 Publications, pp. 31-44.

892 Thordarson, T., Self, S., 1993. The Laki (Skaftár Fires) and Grímsvötn eruptions in 1783–1785.
893 Bull. Volcanol. 55, 233-263, doi: 10.1007/BF00624353.

894 Weinberger, R., Lyakhovsky, V., Baer, G., Agnon, A., 2000. Damage zones around en echelon
895 dike segments in porous sandstone. J. Geophys. Res. 105, 3115-3133.

Wesenlund, F., Grundvåg, S.-A., Engelschiøn, V.S., Thießen, O., Pedersen, J.H., 2021. Linking facies variations, organic carbon richness and bulk bitumen content – A case study of the organic-rich Middle Triassic shales from eastern Svalbard. Mar. Pet. Geol. 132, 105168, doi: https://doi.org/10.1016/j.marpetgeo.2021.105168.

Westoby, M.J., Brasington, J., Glasser, N.F., Hambrey, M.J., Reynolds, J.M., 2012. "Structure-from-Motion" photogrammetry: A low-cost, effective tool for geoscience applications. Geomorphology 179, 300-314, doi: http://dx.doi.org/10.1016/j.geomorph.2012.08.021.

Worsley, D., 2008. The post-Caledonian development of Svalbard and the western Barents Sea. Polar Research 27, 298-317, doi: 10.1111/j.1751-8369.2008.00085.x.